aerospace

MDPI

Article

Large Eddy Simulation of the Influences of the Pilot-Stage Structure on the Flow Characteristics in a Centrally Staged High-Temperature-Rise Combustor

Ge Hu, Qiongyao Qin *, Wu Jin and Jianzhong Li

Key Laboratory of Aero-Engine Thermal Environment and Structure, Ministry of Industry and Information Technology, Nanjing University of Aeronautics and Astronautics, 29 Yudao St., Nanjing 210016, China
* Correspondence: qinqiongyao@nuaa.edu.cn

Abstract: Centrally staged combustion technique is often used in the military high-temperature-rise combustor. The pilot-stage structure affects the flow characteristics in the centrally staged combustor, which further affects the performance of ignition, combustion, and emission of military aero-engines. In order to increase the flow capacity of the swirler, the swirler with a non-rotating channel structure was designed. In this work, the influences of the pilot-stage structure on the flow characteristics in the centrally staged high-temperature-rise combustor are investigated. The flow fields of combustors with different pilot-stage swirl numbers (0.44, 0.60, and 0.71) are analyzed by large eddy simulation (LES). The results demonstrate that the primary recirculation zone (PRZ) becomes gradually longer and wider as the pilot-stage swirl number increases. In the combustors with three different pilot-stage structures, the precessing vortex core (PVC) was formed near the shear layer at the outlet of the pilot stage. The PVC frequency decreased from 1670 Hz to 1425 Hz and 1400 Hz with the increase of the pilot-stage swirl number from 0.44 to 0.60 and 0.71, respectively, and the breakdown position of the PVC shifted forward. The proper orthogonal decomposition (POD) and dynamic mode decomposition (DMD) methods are used to analyze the dynamic flow fields. It was observed that the corresponding frequency of the main pulsation structure decreased, and the flow instability was aggravated with the increase of the pilot-stage swirl number. The results deepen the understanding of the influences of the pilot-stage structure on the flow characteristics in the centrally staged high-temperature-rise combustor.

Keywords: centrally staged high-temperature-rise combustor; large eddy simulation; unsteady characteristics; precessing vortex core; mode decomposition

check for updates

Citation: Hu, G.; Qin, Q.; Jin, W.; Li, J. Large Eddy Simulation of the Influences of the Pilot-Stage Structure on the Flow Characteristics in a Centrally Staged High-Temperature-Rise Combustor. *Aerospace* **2022**, *9*, 782. https://doi.org/10.3390/aerospace9120782

Academic Editor: Eugenio Giacomazzi

Received: 28 October 2022
Accepted: 29 November 2022
Published: 1 December 2022

1. Introduction

With the increase of the thrust-to-weight ratio of aero-engine for military aircraft, the combustor is developing towards the direction of high-temperature rise and high heat capacity combustion [1–3]. In order to solve the contradiction between the high-power smoke from the high-temperature-rise combustor and the lean-fuel flameout of idling rating, the centrally staged combustion technique is proposed. The centrally staged combustor can be implemented by means of a staged supply of air and fuels, thereby extending the stable working range and improving the combustion performance [4,5]. It has become a feasible technical solution for the next generation of the high-temperature-rise combustor. Combustion performance is closely related to the flow characteristics. Consequently, the influences of the pilot-stage structure on flow characteristics in the centrally staged high-temperature-rise combustor is essential.

The centrally staged combustor has been studied as the advanced combustion technique by many scholars. Mongia et al. [6–9] designed a variety of centrally staged high-temperature-rise combustors, the temperature rise reached 1100–1650 K, and the performance reached expectations. At the same time, Mongia et al. designed a twin annular premixing swirler (TAPS) by using the centrally staged combustion technique for low-emission combustion, which was successfully applied to the GENx engine [10,11], reducing NOx emissions by more than 50%. Dhanuka et al. [12,13] revealed that there was a step vortex between the main stage and the pilot stage in the flow field of a TAPS combustor. The main- and pilot-stage jets sheared and mixed with each other downstream of the step vortex, forming a layered flame during combustion. The shear layer could effectively reduce the fuel-air velocity at the tail of the pilot-stage, and the released combustion heat changed significantly the PRZ structure of the TAPS combustor. However, it had little effect on the lip recirculation zone (LRZ) [14]. Lin et al. [15–18] investigated the airflow, thermoacoustic oscillation, and ignition characteristics of an internally staged combustor from the perspectives of the primary combustion level structure, the limited domain of the flame tube, and the air-fuel ratio. They confirmed that the flow field structure of the centrally staged combustor was more complex than that of conventional combustors. Compared to the conventional combustion organizational techniques, all the combustion air of the centrally staged combustor enters from the head, the proportion of cooling and mixing air can be reduced. Therefore, the design of the swirler has an important effect on the performance of the centrally staged combustor. Overall, the studies have mainly focused on improving the performance of centrally staged combustors from the perspectives of optimizing the main-stage structure, the combustor pneumatic parameters, and the fuel supply structure. However, the pilot-stage structure is another important component of the swirler, it affects the flow characteristics, which further affects the performance of ignition, combustion, and emission.

The airflow through the swirler can generate centrifugal forces, develop a negative pressure gradient, and cause a vortex rupture, leading to the formation of the recirculation zone. It shows that the formation of a primary recirculation zone (PRZ) depends on vortex strength and combustor structure. The flow in the PRZ is usually associated with a high strain rate and strong turbulence intensity [19–22], and it is often accompanied by turbulent coherent structures that cause periodic flows. The precessing vortex core (PVC) is a typical coherent structure, which usually appears near the outlet of the swirler and is located in the shear layer of the recirculation zone. It may lead to large fluctuations in the pressure field and affect the combustion performance. Wang et al. [23] reported that the unsteady flow at the outlet of the swirler is related to the periodic movement of the PVC, and the combination of all stages swirler affects significantly the structure of the primary recirculation zone, the shearing effect, and PVC frequency. Liu et al. [24] reported that the PVC captured in the pilot stage induces the asymmetric azimuthal flow instabilities, and the dominant energetic flow is damped rapidly downstream of the pilot stage. Dynamic modal analysis methods have been used to analyze unsteady flow dynamics and understand the complex structure and mechanisms of swirling flow. The most commonly used mode decomposition methods are proper orthogonal decomposition (POD) and dynamic mode decomposition (DMD). In POD, the time sequence of the flow field is decomposed into a coherent structure with a certain energy level [25,26]. POD was used to extract dominant flow features in the multiswirling flow. It showed dominant high-frequency modes in the pilot stage [24]. DMD was proposed by Schmid and applied to unsteady flow analysis [27]. The best feature of DMD is that each obtained mode contains a single information packet of frequency and growth/decay rate. Compared to POD, which adopts order reduction for the flow field, this feature of DMD that can obtain modal characteristics and dynamic information simultaneously endows it with the unique advantage of spatio-temporal coupling.

In this study, the unsteady flow characteristics in the self-designed centrally staged high-temperature-rise combustor with different pilot-stage swirl numbers are investigated by LES. Moreover, the POD and DMD methods are introduced to extract the flow field characteristics, and the effects of the pilot-stage swirl number on the flow characteristics are explored based on the frequency resolution characteristics, vortex structure identification, and modal analysis. This work deepens the understanding of the influences of the pilot-stage structure on flow characteristics in the centrally staged high-temperature-rise combustor.

2. Materials and Methods

2.1. The Swirler Structure

Figure 1 illustrates the swirler structure of the centrally staged high-temperature-rise combustor investigated in this paper. Based on the conceptual design of zonal combustion of the main and pilot stages, the swirler structure mainly comprises a main stage and a pilot stage. The main stage consists of a swirler, a multi-point direct-injection-type nozzle, and a convergent outlet. The main-stage swirler includes a swirling part composed of several blades and a non-swirling part composed of a non-rotating channel to increase the flow capacity of the swirler. The pilot stage consists of a swirler, a centrifugal nozzle, and a convergent outlet. The main- and pilot-stage swirlers have the same swirling direction.

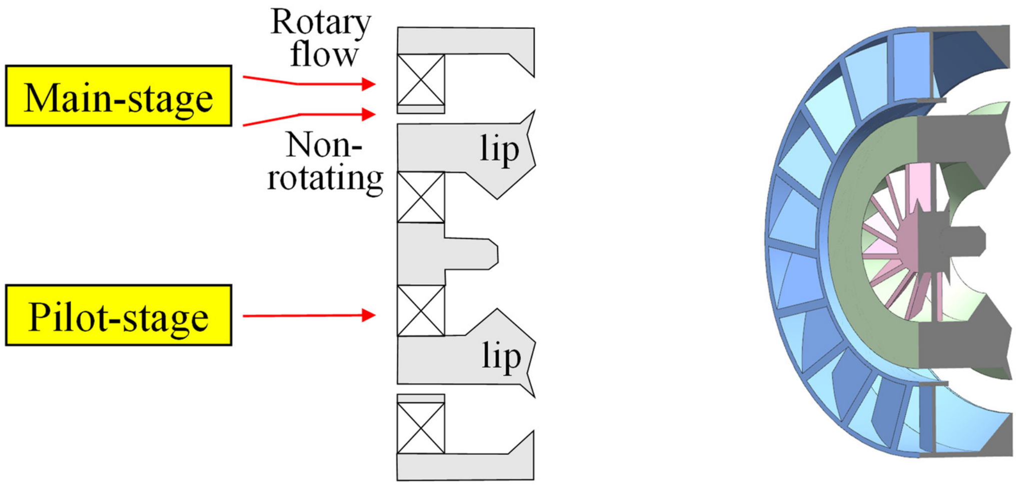

Figure 1. The swirler structure of the centrally staged high-temperature-rise combustor.

The most important parameter used to characterize vortex flow is the swirl number S. For axial swirlers, the swirl number S is defined as:

$$S = \frac{G_m}{G_x R_{eo}} = \frac{2}{3}\tan\theta\left[\frac{1-\left(\frac{R_{ei}}{R_{eo}}\right)^3}{1-\left(\frac{R_{ei}}{R_{eo}}\right)^2}\right] \quad (1)$$

where R_{ei} is the inner radius of the blades and θ is their dip angle.

On the premise of maintaining the effective area of the swirlers at all stages unchanged, geometric parameters of the pilot module swirler, such as the blade angle, blade number, and channel inner and outer diameters, were adjusted to change the swirl number S of the pilot-stage. Thus, three research schemes with pilot-stage swirl numbers of 0.44, 0.60, and 0.71 were proposed; the specific parameters are listed in Table 1.

Table 1. Parameters of the three different swirlers.

Parameters	Swirl Number of Pilot-Stage		
	0.44	**0.60**	**0.71**
Blade angle/(°)	32°	40°	48°
Outer radius of inlet/mm	21.2	22.5	24.3
Inner radius of inlet/mm	6	6.5	7

2.2. Numerical Method

The flow characteristics of the centrally staged combustor with three different pilot-stage swirl numbers were determined using LES. Based on the work by Zhang et al. [28], a numerical study on the transient flow and combustion in an SGT-100 combustor was performed using the LES-WMLES model, and the calculation results reproduced adequately the test results in [29]. On this basis, it can be considered that the LES-WMLES model is suitable for the unsteady calculation of the combustor with a strong swirling flow. Hence, this paper adopted the LES-WMLES model. The simulations were performed using Ansys Fluent. The LES method can accurately capture the transient information of the flow field, solve the large-scale turbulence directly, and solve the remaining small-scale turbulence by a sub-grid model. The filtered Navier–Stokes equation can be expressed as:

$$\frac{\partial\overline{\rho}}{\partial t}+\frac{\partial\overline{\rho}\widetilde{u}_i}{\partial x_i}=0 \tag{2}$$

$$\frac{\partial\overline{\rho}\widetilde{u}_i}{\partial t}+\frac{\partial\left(\overline{\rho}\widetilde{u}_i\widetilde{u}_j\right)}{\partial x_j}=-\frac{\partial\sigma_{ij}}{\partial x_j}-\frac{\partial\overline{p}}{\partial x_i}+\frac{\partial\tau_{ij}^{sgs}}{\partial x_j} \tag{3}$$

$$\frac{\partial\overline{\rho}\widetilde{Y_{\mathrm{k}}}}{\partial t}+\frac{\partial\left(\overline{\rho}\widetilde{Y}_k\widetilde{u}_j\right)}{\partial x_j}=\frac{\partial}{\partial x_j}\left(\overline{\rho}\widetilde{D}_k\frac{\partial\widetilde{Y}_k}{\partial x_j}\right)-\frac{\partial}{\partial x_j}\left(\overline{\rho}\widetilde{u_jY_k}-\overline{\rho}\widetilde{u}_j\widetilde{Y}_k\right)+\overline{w}_k \tag{4}$$

$$\frac{\partial\overline{\rho}\widetilde{h}}{\partial t}+\frac{\partial\left(\overline{\rho}\widetilde{u}_j\widetilde{h}\right)}{\partial x_j}=\frac{D\overline{p}}{Dt}-\frac{\partial}{\partial x_j}\left(\overline{\rho}\widetilde{u_jh}-\overline{\rho}\widetilde{u}_j\widetilde{h}\right)+\frac{\partial}{\partial x_j}\left(\overline{\rho\alpha}\frac{\partial\widetilde{h}}{\partial x_j}\right)+\overline{\tau_{ij}\frac{\partial u_i}{\partial u_j}} \tag{5}$$

In the LES model, it can be determined with the Boussinesq assumption:

$$\tau_{ij}^{sgs}=\overline{\rho}\left(\widetilde{u_iu_j}-\widetilde{u}_i\widetilde{u}_j\right)=-2\mu_{sgs}\widetilde{S_{ij}^{D}}+\frac{2}{3}\overline{\rho}k\delta_{ij} \tag{6}$$

In order to close the governing equation, this paper selects the Algebraic Wall-Modeled LES model (WMLES). It uses the RANS method to simulate the flow field inside the boundary layer, while it uses the LES method to simulate the flow field outside the near wall area. The eddy viscosity is defined as:

$$\mu_t=\min\left[(\kappa d_w)^2,\left(C_{Smag}\Delta\right)^2\right]\cdot S\left\{1-e^{\left[-\left(y^+/25\right)^3\right]}\right\} \tag{7}$$

where S is the strain rate, d_w is the distance between the point and the wall. Filter size Δ is selected according to the flow field conditions:

$$\Delta=\min(\max(C_w\cdot d_w;C_w\cdot h_{max};h_{wn});h_{max}) \tag{8}$$

where C_w = 0.15, h_{max} is the maximum step size of the wall grid, h_{wn} is the mesh step size of the extension wall's normal direction.

2.3. Boundary Conditions

Since the airflow velocity in the combustor is relatively low, the air was treated as incompressible ideal gas for calculation. The working pressure was 0.9 MPa, the temperature was 700 K, and at the inlet, a velocity of 10 m/s was set. The pressure outlet was adopted, and in this case, the total pressure loss coefficient of the combustor was 4%. In the calculation process, the time step was dynamically adjusted, and the maximum time step was 10^{-5} s. Thus, the CFL number was less than 0.5. In order to make the LES converge faster, Reynolds-averaged Navier–Stokes (RANS) simulation was performed first to obtain the steady-state flow characteristics. After the RANS simulation converged, the RANS simulation was converted into the LES simulation. Based on the combustor length and the average inlet velocity, the flow characteristic time Δt was estimated to be about 27.5 ms. After two characteristic time periods, unsteady flow data were collected. The statistical process lasted for 10 Δt, i.e., 0.275 s.

2.4. Grid Partition

Figure 2 illustrates the grid partition of the simulation model. The air intake section and the flame tube were 1.28 × 1.96 (the combustor size was expressed as the result of 100 mm normalization) rectangular, and the restricted ratio, i.e., the ratio of the flame tube section area to the swirler outlet area, was 3.82. The axial position of the swirler inlet was z = 0, the swirler outlet was z = 0.35, and the outlet of the combustor was z = 2.45. A polyhedral grid was adopted for the entire 3D computational domain, and the grids in the swirler zone were denser in order to improve computational accuracy. To reduce the effect of the grid partition factors on the calculation results, the dimension, density, and change ratio of the grids in the combustor were consistent for all models. In the models, the points P (z = 0.5, y = 0.1) and Q (z = 0.5, y = 0.4) were located at the outlets of the pilot and main stages on Plane-M, respectively.

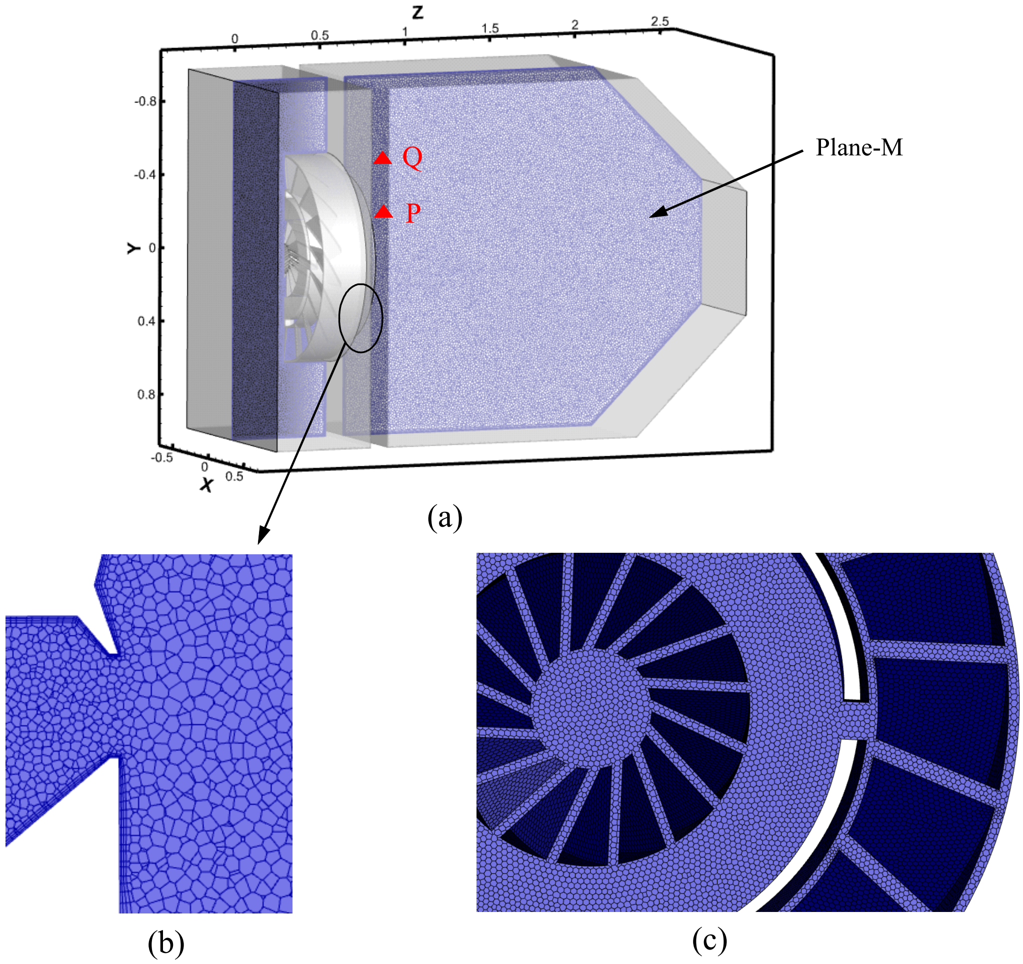

Figure 2. Grid distributions. (**a**) Computational grid, (**b**) grid around the swirler outlet, and (**c**) grid on the surface of swirler.

By taking the model with a pilot-stage swirl number *S* of 0.44 as an example, Figure 3 shows the axial velocity and pressure distribution along the path at Z = 0.7 on Plane m for the three meshes with different dimensions. In general, the position Z = 0.7 on Plane m is near the swirler outlet and the airflow runs through the main characteristic vortices of the centrally staged combustor. Consequently, the distribution can effectively characterize the flow inside the combustor. In the compromise of spatial resolution and computational cost, the computational domain was divided into 3.4 million elements in order to solve this multi-scale problem.

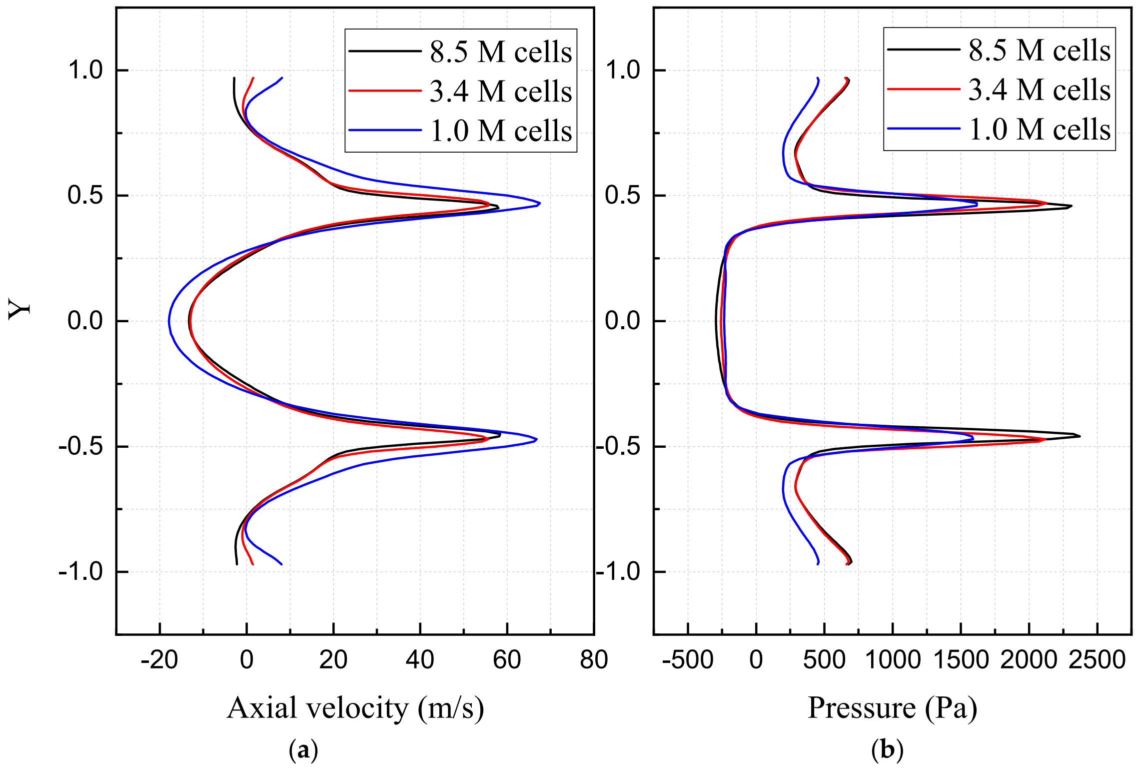

Figure 3. Grid sensitivity analyses. (**a**) Axial velocity. (**b**) Pressure.

Figure 4 depicts the energy spectral graph obtained by a Fourier analysis of the instantaneous axial velocity at point P at the pilot-stage outlet. It can be observed that the variation relationship between amplitude and frequency conforms to the −5/3 law in the inertial subregion of the Kolmogorov–Obukhov Theory [30]. This indicates that the grid partition method used in this paper can effectively distinguish the turbulent pulsation in the combustor. Therefore, the abovementioned grid partition parameters were used to divide the computational domain of the combustors with three different structures.

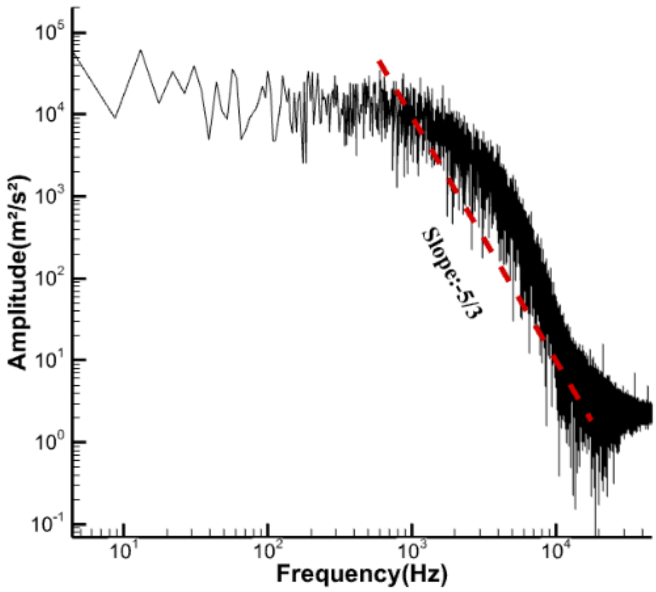

Figure 4. Spectrum of instantaneous axial velocity at point P.

2.5. Post-Processing Method

In this study, the POD and DMD methods were introduced in order to conduct a dimension reduction analysis of the LES flow field results. Both POD and DMD are dataset-based modal analysis methods, which can transform the flow field data at the moment $\{t_1, t_2, \cdots, t_N\}$ into a column vector x_i. The reconstruction was achieved by preserving the corresponding relationship between the coordinates of spatial points and vector elements. For multivariable snapshots, only the corresponding relationship between vector elements and variables needs to be maintained. The dimension number of x_i can be denoted as M, and it is assumed that there are N time moments in total; that is, the number of samples is N. Thus, all data samples constitute a two-dimensional matrix $U_{M\times N}$, $U_{M\times N} = [x_1, x_2, \cdots, x_N]$. In practical applications, time series data require a sufficiently high number of sampling space points, i.e., $M \gg N$. The essence of the POD and DMD methods is to seek basis functions of different properties for the data samples $U_{M\times N}$. The projections of the target snapshot data x_i on these two different basis functions are defined as POD and DMD modes, respectively.

The POD method requires pre-processing treatment. Here, x_i can be expressed by the average and pulsation quantities as:

$$x_i = \overline{x} + \widetilde{x_i} = \frac{1}{N}\sum_{j=1}^{N} x_j + \widetilde{x_j} \tag{9}$$

Subsequently, the pulsation snapshot sequence $\widetilde{U_{M\times N}} = [\widetilde{x_1}, \widetilde{x_2}, \cdots, \widetilde{x_n}]$ is constructed based on the snapshot pulsation quantity. Since this study mainly focuses on the unsteady flow structure in the combustor, the average values of the snapshots were removed and only the pulsation values of the snapshots were decomposed by POD. The essence of POD is to transform the time-domain signals into frequency-domain signals by Fourier transform according to the Wiener–Khinchin Theorem, and then complete the decoupling of the time–space correlation in the frequency domain. POD seeks a set of orthogonal bases $\{\phi_1, \phi_2, \cdots, \phi_N\}$ defined on a Hilbert space such that the projection of x_i onto them is optimal in the least-squares sense. In this study, a POD based on singular value decomposition is adopted, which can significantly reduce the computation amount compared to the direct POD method proposed by Lumley [25]:

$$U' = U \cdot S \cdot V' = \sum A_i(t) \cdot \phi_i(x) \tag{10}$$

where $A_i(t)$ is the time evolution information corresponding to a certain mode, and $\phi_i(x)$ is the corresponding i-th POD mode.

A Koopman operator A is introduced in the DMD method in order to the mapping of the $U_i \sim U_{i+1}$ snapshot:

$$U_{i+1} = A * U_i \tag{11}$$

The key is to solve matrix A. In this study, the similarity transformation order reduction method based on POD proposed by Schmid is used to solve the matrix A. By using the flow field snapshots at the moments from 1 to N, two snapshot matrices $X = [x_1, x_2, \cdots, x_{N-1}]$ and $Y = [x_2, x_3, \cdots, x_N]$ can be constructed. Thus, the following relationship can be obtained:

$$Y = [x_2, x_3, \cdots, x_N] = [Ax_1, Ax_2, \cdots, Ax_{N-1}] = AX \tag{12}$$

For matrix X, there is an order-reduced matrix $\widetilde{A}$ similar to matrix A, which can replace the high-dimensional matrix A to make $X = U\Sigma V^H$, where Σ is a diagonal matrix and its diagonal elements have r singular values. Thus, the following relationship can be obtained:

$$\widetilde{A} = U^H A U = U^H Y V \Sigma^{-1} \tag{13}$$

The matrix $\widetilde{A}$ contains the main characteristic values of matrix A. The j-th characteristic value of $\widetilde{A}$ is denoted as μ_j and the proper vector as ω_j. Subsequently, the j-th DMD mode is $\phi_j = U\omega_j$. Based on the characteristic values, the growth rate and change frequency of the system can be obtained as well.

The snapshot at an arbitrary moment can be estimated as follows:

$$x_i = Ax_{i-1} = U\widetilde{A}U^H x_{i-1} = UWNW^{-1}U^H x_{i-1} = UWN^{i-1}W^{-1}U^H x_1 \tag{14}$$

where W is a matrix in which the column vector is the proper vector ω_j, and N is a diagonal matrix which contains the singular values of the matrix $\widetilde{A}$.

Each column of ϕ is defined as one DMD mode; that is, ϕ = UW. The mode amplitude is defined as $\alpha = W^{-1}U^H x_1$, and the DMD modes are ranked according to the mode amplitude. Thus, the following relationship can be obtained:

$$x_i = \phi\Lambda^{i-1}\alpha = \sum_{j=1}^{r} \phi_j (\mu_j)^{i-1}\alpha_j \tag{15}$$

3. Experimental Validations

3.1. Experimental Settings

Particle imaging velocimetry (PIV) was used to capture the cold flow field in a combustor with a pilot-stage swirl number of S = 0.44. The experimental system mainly included the combustor, air supply system, and PIV flow field measurement system (Figure 5). The air was stored in a high-pressure bottle to ensure stable airflow before entering the combustor. A total pressure rake was installed at the trailing end of the inlet pipeline rectification section to determine the total pressure at the inlet and outlet of the combustor; the measurement uncertainty was 1%. The inlet flow rate was acquired through an orifice flowmeter with a measurement uncertainty of 2%. The MicroVec SM3-8M200 PIV system was adopted, it includes an ND-YAG double-pulse laser with 532 nm wavelength and 200 mJ working on the 15 Hz frequency and a 2360 × 1776 pixels charge-coupled device (CCD) camera. The time interval between the two laser pulses was set to 5–8 µs for the flow conditions studied. The valid area of the PIV post-processing is 170 × 100 mm. The estimated uncertainty is about 8% in the wake region of the swirler [31]. The essence of PIV measurement is to characterize the flow structure by acquiring the flow characteristics of the tracer particles. Stokes number (*Stk*) is introduced as the criterion for selecting tracer particles [32]. The *Stk* is defined as the ratio of the particle relaxation time to the fluid characteristic time, which represents the ratio of the particle inertia effect to the diffusion effect. Its calculation equation is as follows:

$$Stk = \tau_f / \tau_p \tag{16}$$

when $Stk < 1$, particle diffusion is more dominant than the inertial force; thus, the PIV testing results are more reliable. To ensure that $Stk < 1$ during the test, the tracer particles were introduced 1 m upstream of the air intake section. Al_2O_3 particles with a size of 2 µm were selected as the tracer particles.

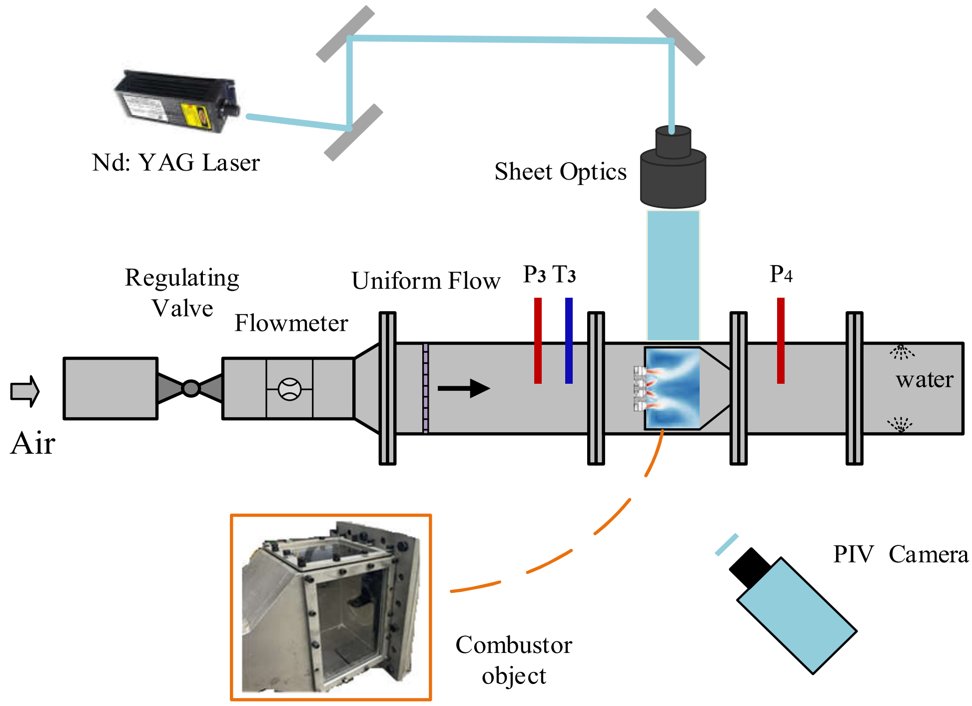

Figure 5. The PIV flow field measurement system.

3.2. Experimental Result Validation

The PIV flow field experiment was performed under the conditions of 1 atm and 300 K. To verify the accuracy of the numerical calculation in predicting the flow structure of the combustor, the LES method was performed with the same boundary conditions, same computational grids, and under the same working conditions as those in the PIV test. Figure 6a shows the average flow field on both the experiment and simulation. It can be found that the flow field structure is similar in the two cases. Figure 6b shows the axial velocity distributions at different axial positions of the cold time-average flow field obtained from the PIV test as well as the time-average results obtained by LES. It can be observed that the velocity profiles captured by LES agreed well with the PIV measurement results. Furthermore, the corresponding relationship between the data points measured by the PIV system and those predicted by the numerical simulation was verified, and the correlation coefficient (R^2) values between the numerical simulation and experimental results were analyzed. Table 2 lists the correlation coefficient values of the axial velocity at different axial positions obtained by PIV and LES. It can be seen that the correlation coefficients between the simulated velocity component and the experimentally measured velocity component were both greater than 82%, indicating the high reliability of the numerical simulation results. The reason for the gap of errors between LES and PIV in Figure 6b may be that the primary recirculation zone of the combustor is small, a small number of tracer particles enter the primary recirculation zone during the experiment, resulting in a certain error in the discrimination of the PIV system. Therefore, the grids and methods used for the LES in this study can efficiently simulate the combustor flow field.

Table 2. R^2 of axial velocity.

Z	0.55	0.75	0.95
R^2(%)	92	87	82

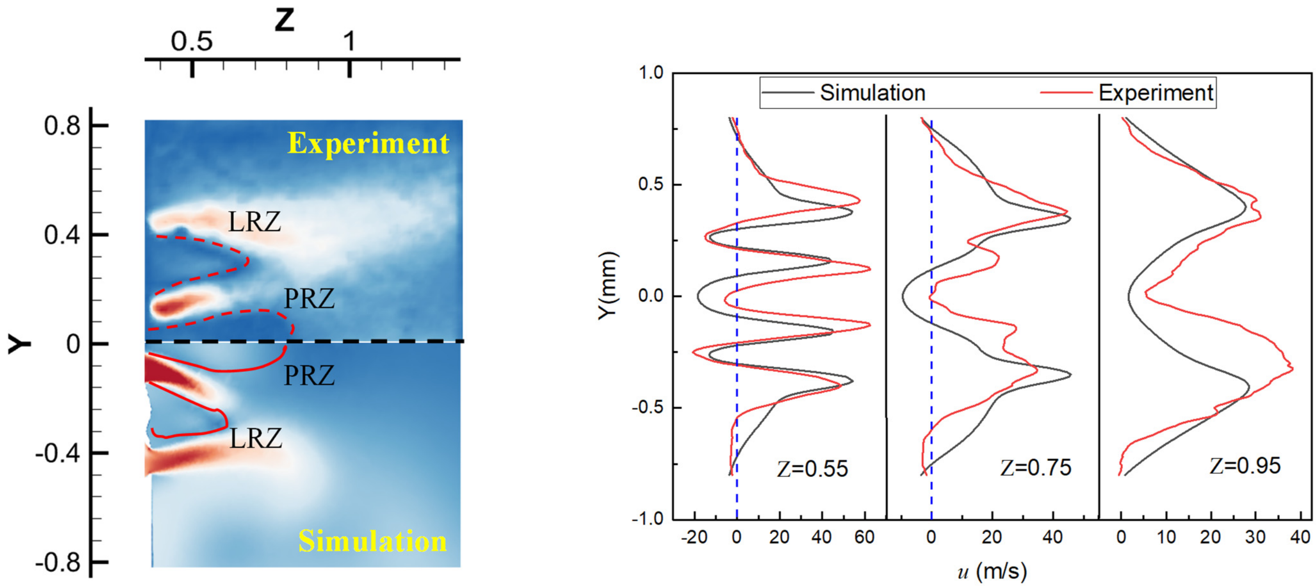

(a) (b)

Figure 6. The flow characteristics on both experiment and simulation for validation. (**a**) the average flow field. (**b**) the axial velocity distributions.

4. Results and Discussion

4.1. Effects of Pilot-Stage Structure on the Time-Average Vortex Structure

The generation of a coherent structure depends mainly on the swirling intensity at the outlet of the swirler, which can lead to the formation of a PRZ surrounded by the inner shear layer [33]. The Strouhal number is a similarity criterion used to characterize the periodicity of flow, which is defined as:

$$Sr = \frac{lf}{v} \tag{17}$$

where l is the characteristic size of the structure, and f and v are the frequency and average flow velocity at the junction, respectively. Huang et al. [34] reported that the periodic flow frequency of the PVC or vortex shedding in cold swirling flow is positively correlated with the average velocity. On this account, in this study, the effects of different pilot-stage swirl numbers on the unsteady flow characteristics are investigated under the same inlet velocity.

The time-average results by LES can represent the characteristics of the time-average flow in the combustor and reflect the main structure of the vortex. Since the LES process is sufficiently long, the airflow in the combustor can be fully developed, and the structure of the time-average flow field is basically symmetric about the central axis; thus, only half of the flow field is presented in this study. Figure 7 shows the time-average flow field of the combustors with three different pilot-stage structures on Plane-M under an inlet velocity of 10 m/s. As it can be observed, the main and pilot module jets exhibited a stratified flow state, forming a typical stratified vortex structure of CRZ, LRZ, and PRZ. Due to the mixing effect of the main-stage swirling flow and the non-swirling air, the main-stage jet moved downstream along the axial direction, and basically did not participate in the formation of recirculation zones. On the contrary, the jet at the outlet of the pilot-stage swirler possessed strong tangential velocity, which could expand outward under the action of centrifugal force. Furthermore, the decrease of the jet axial velocity and the jet radial expansion could make the air flow produce a pressure gradient along the axial direction, and facilitate the formation of a stable PRZ, which was conducive to flame stability. The "step" structures between the main- and pilot-stage outlets as well as between the main-stage outlet and the flame tube wall could produce low-pressure zones and form an LRZ and a CRZ, respectively, effectively achieving the purpose of staged airflow. With the increase of the pilot-stage swirl number, the centrifugal force was enhanced, and the jet tension angle of the pilot stage became larger. Consequently, the LRZ was squeezed to be smaller, while the length and width of the PRZ were increased.

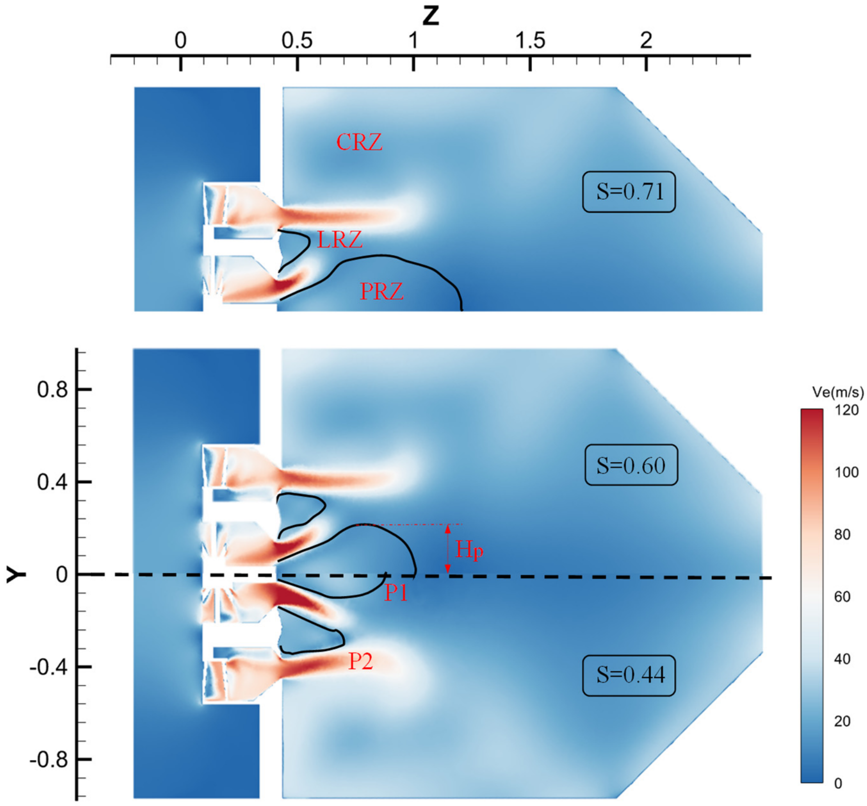

Figure 7. Flow fields of Plane-M with different pilot-stage swirl numbers.

To quantitatively describe the characteristics of the recirculation zones in the centrally staged combustor, the main characteristic parameters are defined as follows: P1 represents the posterior stagnation point of the PRZ, which describes its axial length; P2 represents the posterior stagnation point of the LRZ, which describes its axial length (L denotes to the axial distance from the swirler outlet); Hp represents the maximum distance from the PRZ to the central axis of the combustor, which describes the PRZ width. Table 3 lists the characteristic parameters of the recirculation zones for different pilot-stage structures. With the increase of the pilot-stage swirl number, the centrifugal force of the jet at the pilot-stage outlet was increased, which was conducive to the establishment of an adverse pressure gradient and the radial expansion of the pilot module jet. After the pilot-stage jet was mixed with the main-stage jet, the flow field exhibited an increasing PRZ width and a retroposition of the stagnation point, i.e., the PRZ became gradually wider and longer. Moreover, the pilot-stage jet could compress the LRZ, the length of which became gradually smaller. Thus, the squeezing effect of the corner vortex on the main-stage jet was weakened, promoting the development and expansion of the PRZ.

Table 3. Parameters of the three different combustors.

Parameters	**Pilot Swirl Number**		
	0.44	**0.60**	**0.71**
L_{p1}	0.62	0.75	0.79
L_{p2}	0.25	0.17	0.13
H_p	0.12	0.14	0.19

4.2. Effects of Pilot-Stage Structure on Vortex Dynamic Evolution

The breakdown process of large-scale vortices plays an important role in the mixing, transport, and instability of turbulent flows, while the PVC is the most typical coherent structure in a swirling flow field. Figure 8 presents the instantaneous pressure isosurface (P = −30,000 Pa) in the combustor. As it can be observed, for all centrally staged swirl flows, there are PVCs rotating clockwise along the axial direction in the combustor, and the rotation direction is the same as that of the blades of the pilot-stage swirler. PVCs exist only near the shear layer at the outlet of the pilot stage, and the axial velocity gradient around the shear layer is high. PVCs develop downstream along the flow field, gradually break, and finally disappear. The increase of the pilot-stage swirl number can lead to an increase in the shear stress of the flow field. Consequently, the location of vortex breakdown moves clearly upstream of the combustor. The solid black line in Figure 8 represents the 3D streamline of the average velocity field passing through the vortex structure. It can be observed that the vortex axis of each combustor had an orthogonality relation with the streamline of the average velocity field in space. This suggests that the PVC structures near the shear layer of the pilot-stage outlet were all generated by the Kelvin–Helmholtz instability in the shear layer [35].

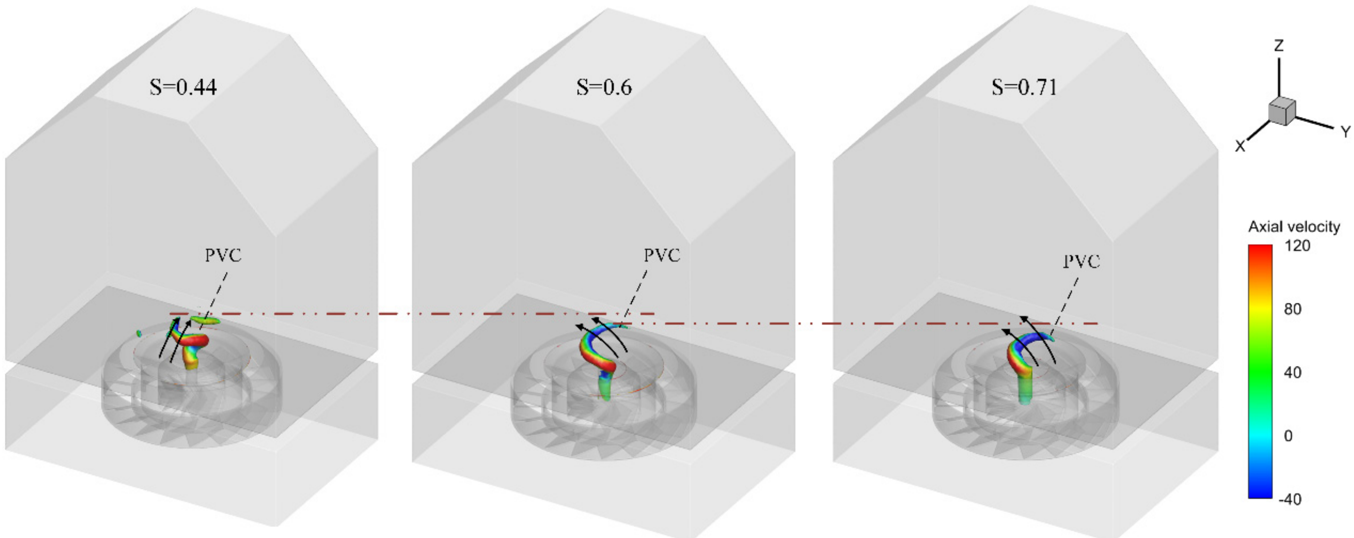

Figure 8. PVC in the combustor with different pilot−stage swirl numbers (colored by axial velocity).

Figure 9 demonstrates the frequency spectra of the instantaneous axial pulsation velocity u' at different monitoring points of the centrally staged combustor by fast Fourier transform (FFT). For the three models, there was a dominant frequency in the axial pulsation velocity spectrum of point P at the pilot-stage outlet; however, there was no obvious dominant frequency in the axial pulsation velocity spectrum of point Q at the main-stage outlet. This means that the main pulsation zones were distributed near the PRZs wrapped by the inner shear layer. The pulsating dominant frequencies decreased gradually with the increase of the pilot-stage swirl number, i.e., 1670, 1425, and 1400 Hz, respectively.

The continuous equally spaced flow snapshots of the plane-M obtained by LES were processed by POD. The samples comprised 2000 instantaneous flow fields, and the frequency resolution was 5 Hz. Here, the mean flow field is denoted as the zero-order mode. Figure 10 illustrates the energy distribution of each mode calculated based on the proper values of the orthogonal decomposition for the flow field snapshots from the three different centrally staged combustors. It can be seen that, in all cases, the energy distribution of the different combustor flow fields presented a "long-tail" pattern. The energy proportion of the first-order mode accounted for about 8% of the different pilot-stage swirl numbers, and it increased slightly with the increase of the pilot-stage swirl number. These results confirmed that the coherent structures captured by POD are small fluctuations near large-scale structures, it can be deduced that the downstream flow field pulsation can be enhanced by increasing the pilot-stage swirl number.

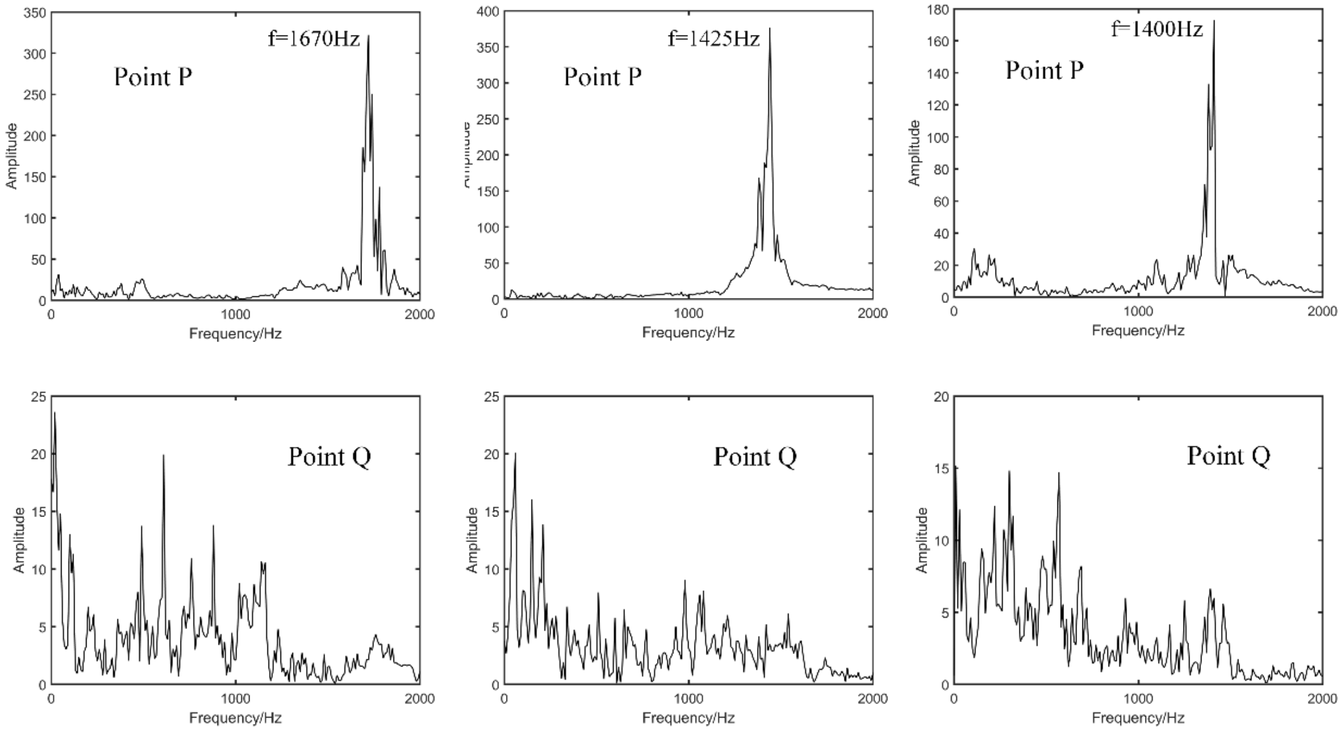

Figure 9. Spectrogram of axial pulsation velocity at different points (left: S = 0.44, mid: S = 0.60, right: S = 0.71).

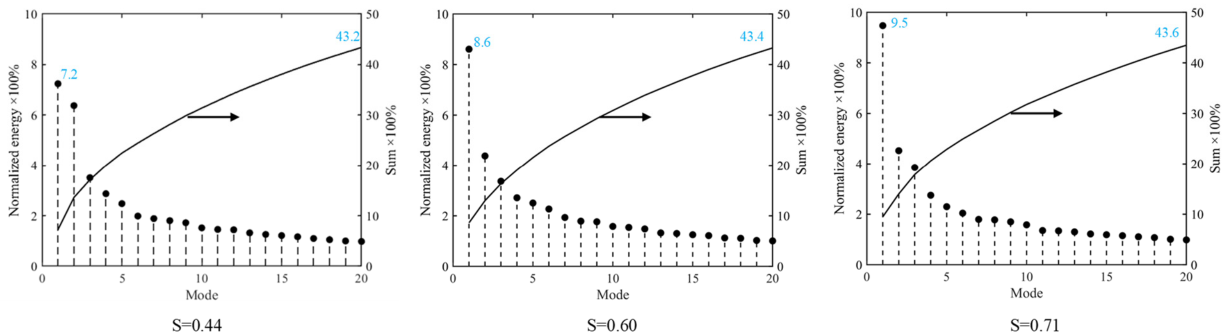

Figure 10. Energy distributions of POD modes.

Figure 11 demonstrates the power spectral densities (PSD) of each modal coefficient time series obtained via POD of the axial velocity field snapshots on Plane m for the three combustors with different pilot-stage structures. For all three structures, an obvious dominant frequency in the first- and second-order time series was found, while the other frequencies could even be ignored completely. Moreover, the dominant frequency was basically consistent with the PVC frequency in the combustor with the corresponding pilot-stage structure. In addition, the frequency spectra of the other modal coefficients no longer exhibited the pattern of extremely high intensity at a certain frequency and negligible intensity at other frequencies. Nevertheless, when S = 0.44, the PSD pattern of the three- and four-order modal time series also exhibited an apparent low-frequency pulsation. This may be attributed to the existence of strong low-frequency pulsation structures in the modes, which can be subsequently verified by the spatial distribution results of each mode. Furthermore, according to Figure 9, the energy proportion sum of the modes after the first four orders of the modes was less than 3%. Hence, the first four orders of the POD modes were selected for the subsequent analyses in this study.

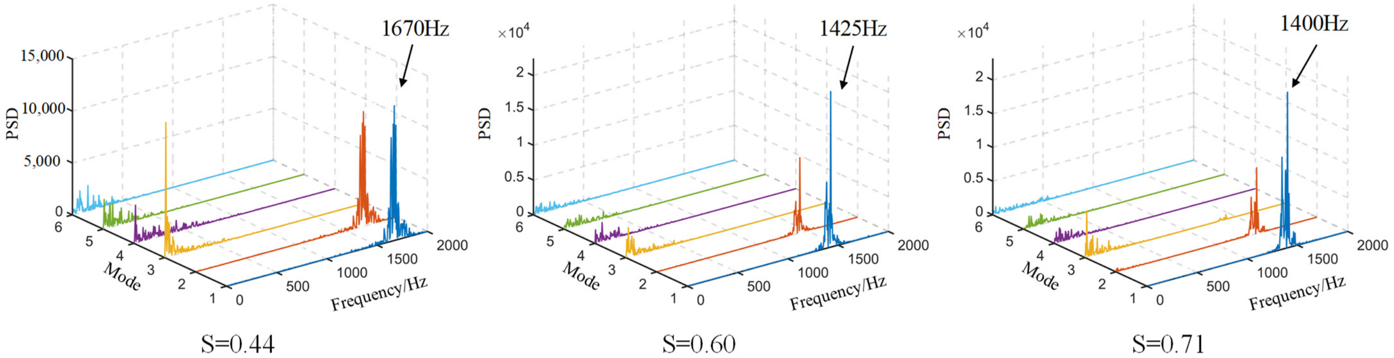

Figure 11. PSD of POD under different flow field snapshots.

Through POD, the first four orders of the modes of the axial velocity field snapshots on Plane m of the three combustors were shown in Figure 12. It was found that there was a phase difference of 90° between the first- and second-order modes, as well as between the third- and fourth-order modes. The first- and second-order modes were mainly distributed near the shear layer of the pilot-stage outlet, whereas the third- and fourth-order modes were distributed over the downstream region of the combustor. The overall structure of each mode did not change with time, while the corresponding energy intensity changed periodically with time, so spatio-temporal decoupling occurred. Since the modes extracted by POD do not have frequency analyticity, the main pulsation structure obtained by POD contains multiple frequencies. Combined with the time coefficient PSD diagrams corresponding to each order of mode, it can be deduced that the first- and second-order modes of each structure corresponded to the high-frequency flow structures in the frequency domain, i.e., the PVC flow structures. This is similar to the phenomenon obtained by the high-speed PIV experiment [36]. It shows that the dominant PVC unsteady motions are located in the inner shear layer of pilot stage. When S = 0.44, the third- and fourth-order modes mainly present low-frequency flow structures. On the other hand, the third- and fourth-order modes for the pilot-stage structures with S = 0.60 and S = 0.71 also contained some high-frequency flow structures in addition to the low-frequency ones, especially for the pilot-stage structure when S = 0.71. These indicate that, by increasing the pilot-stage swirl number, the flow instability in the combustor is aggravated. Thus, the above speculation about the difference in the PSD curves is verified. It should be highlighted that the POD results are only mathematical decomposition results. It can be found that the decomposed modes specifically reflect certain physical phenomena, such as the average flow characteristics as well as those of various vortex systems.

Based on the sequence of the energies of all modes, the energy-frequency diagrams of the first four orders of the modes decomposed by DMD of the axial velocity field snapshots on Plane m of the three combustors with different pilot-stage structures were shown in Figure 13. Since the two adjacent proper values/vectors were conjugate, that is, the real parts were the same and the imaginary parts were opposite, the spatial distributions of the two adjacent modes were the same. Negative and positive frequencies appeared in pairs, and the frequencies of two adjacent modes were opposite to each other. Hence, the modes corresponding to positive frequencies could be used for modal analysis. For the three pilot-stage structures, the first-order modal frequency obtained by DMD was consistent with the main frequency of the first-order modal time series obtained by POD. Only when S = 0.44 was the third-order modal frequency obtained by DMD consistent with the main frequency of the third-order modal time series obtained by POD, exhibiting the characteristics of low-frequency pulsation. When S = 0.60 and S = 0.71, the third-order modes obtained by DMD exhibited the characteristics of high-frequency pulsation.

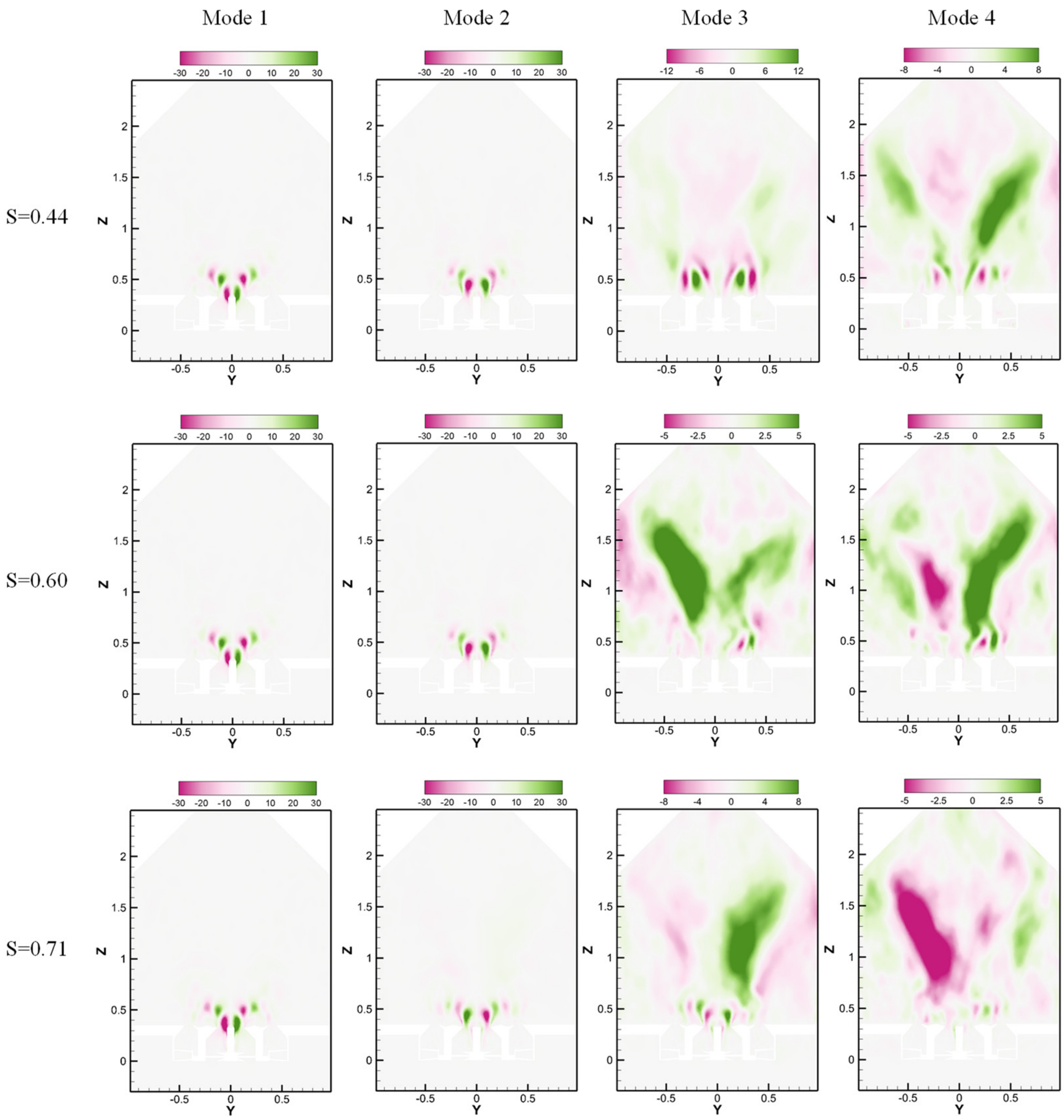

Figure 12. The spatial distribution of the first four modes by POD.

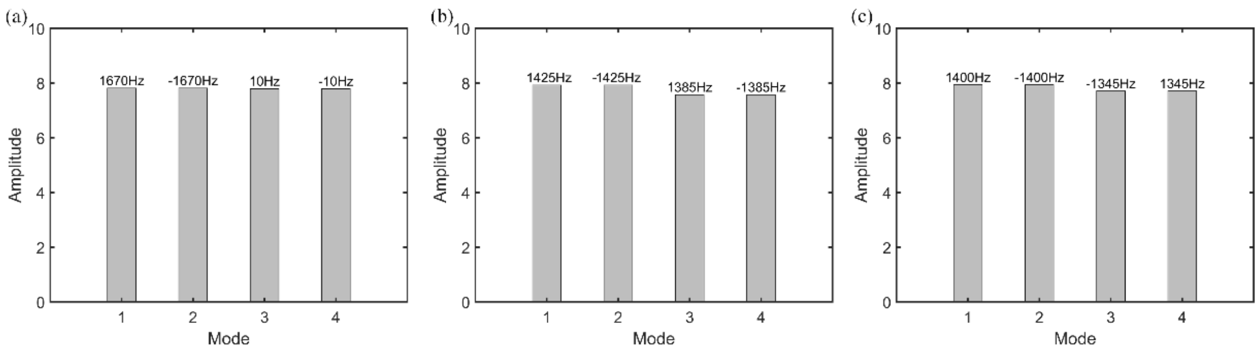

Figure 13. Energy−frequency diagram of the first four modes by DMD ((**a**) S = 0.44, (**b**) S = 0.6, (**c**) S = 0.71).

Figure 14 shows the spatial distribution of the real and imaginary parts corresponding to the first and third orders of the modes obtained by DMD for the three combustors with different pilot-stage structures. It can be observed that there was a corresponding relationship of a 90° phase difference between the real and imaginary parts of the same order of the modes. Due to the spatio-temporal coupling characteristic of DMD, the obtained modes were pulsation structures with a certain single frequency. Consequently, when S = 0.44, the spatial distribution of the real and imaginary parts of the first-order mode reflected the high-frequency pulsation structure, while that of the third-order mode reflected the low-frequency pulsation structure with higher modal energy. When S = 0.60 and S = 0.71, the spatial distributions of the real and imaginary parts of the first- and third-order modes reflected the high-frequency pulsation structures. Based on the transverse comparison between POD and DMD, the real and imaginary parts of the first pair (first and second orders) of POD modes exhibited spatial distributions similar to those of the first-order DMD mode for the three combustors. When S = 0.44, the real and imaginary parts of the third-order mode were significantly different from those of the structures with S = 0.60 and S = 0.71. At this point, the real and imaginary parts of the second pair (third and fourth orders) of POD modes exhibited spatial distributions similar to those of the third-order DMD mode. However, for the structures with S = 0.60 and S = 0.71, no apparent corresponding relationships between the real and imaginary parts of the second pair (third and fourth orders) of POD modes and those of the third-order DMD modes were found. To sum up, the order reduction methods of POD and DMD can facilitate the analysis of complex flow fields, successfully capture and extract their important characteristics, and help to better understand the unsteady flow characteristics of the centrally staged combustor.

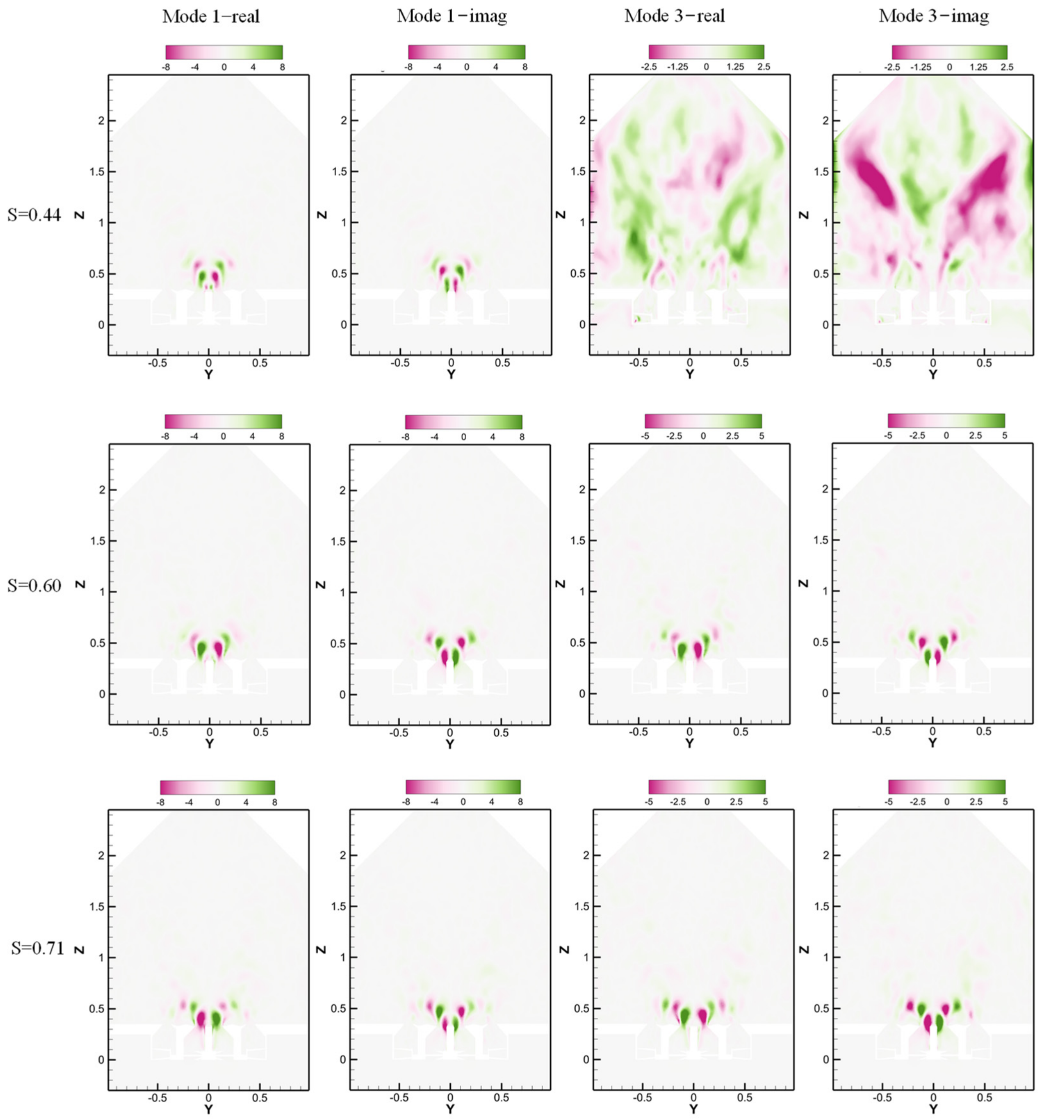

Figure 14. The spatial distribution of the first four modes by DMD.

5. Conclusions

The LES method was used to explore the influences of the pilot stage structure on the flow characteristics in the centrally staged high-temperature-rise combustor. Based on the LES results, the POD and DMD methods were introduced to further analyze the flow field. The main conclusions are as follows:

(1) Increasing the swirl number of the pilot-stage is conducive to the radial expansion of the pilot-stage jet. When the pilot-stage swirl number was 0.44, 0.60, and 0.71, the length of the recirculation zone was 0.62, 0.75, and 0.79, respectively, and its half-height was 0.12, 0.14, and 0.19, respectively.

(2) PVCs were formed at the outlet of the pilot stage in the three combustors with different structures (S = 0.44, S = 0.60, and S = 0.71), and the PVC frequencies were 1670 Hz, 1425 Hz, and 1400 Hz, respectively. The PVC vortex axis and the average velocity field streamline exhibited an orthogonality relation in space, indicating that PVCs are generated due to the Kelvin–Helmholtz instability in the shear layer. The PVC breakdown position shifted forward with the increase of the pilot-stage swirl number.

(3) After the order reduction analysis via POD and DMD, it was determined that the main pulsation structures of the flow field for the three pilot-stage swirl numbers were located near the shear layer of the pilot-stage outlet. The main frequency of the DMD modes, the time series main frequency of the POD modes, and the FFT main frequency of the monitoring point P at the pilot-stage outlet was consistent. The modal analysis results revealed that the increase of the pilot-stage swirl number can enhance the energy of the main pulsation structures and aggravate the instability of the flow field. Therefore, the appropriate pilot-stage structure needs to be combined with the time-average flow field structure and the vortex dynamic evolution characteristics.

(4) Using the spatio-temporal decoupling characteristics of POD and the spatio-temporal coupling characteristics of DMD, flow field analyses can be conducted from different perspectives to capture different flow structure characteristics, which can be helpful to understand the flow characteristics in the centrally staged high-temperature-rise combustor.

Author Contributions: Conceptualization, G.H. and Q.Q.; Methodology, J.L.; Software, G.H.; Validation, G.H. and W.J.; Investigation, G.H.; Resources, Q.Q.; Data curation, W.J.; Writing—original draft preparation, G.H. and Q.Q.; Writing—review and editing, Q.Q. and J.L. All authors have read and agreed to the published version of the manuscript.

Funding: The authors would like to acknowledge support from the National Science and Technology Major Project (Grant Number 2017-III-0002-0026), National Science and Technology Major Project (Grant Number 2019-III-0014-0058).

Data Availability Statement: The data used to support the findings of this study are available from the corresponding author upon request.

Conflicts of Interest: The authors declare no conflict of interest.

Nomenclature

PVC	Precessing vortex core	POD	Proper orthogonal decomposition
LES	Large eddy simulation	DMD	Dynamic model decomposition
PIV	Particle image velocimetry	LRZ	Lip recirculation zone
PRZ	Primary recirculation zone	CRZ	Corner recirculation zone
Stk	Stokes number	FFT	Fast fourier transform
Sr	Strouhal number	PSD	Power spectral densities

References

1. Lieuwen, T.C.; Yang, V. *Gas Turbine Emissions: Contents*; Cambridge University Press: Cambridge, UK, 2013.
2. Bahr, D.W. Technology for the design of high temperature rise combustors. *J. Propuls. Power* **2012**, *3*, 179–186. [CrossRef]

3. Li, J.; Chen, J.; Jin, W.; Yuan, L.; Hu, G. The design and performance of a RP-3 fueled high temperature rise combustor based on RQL staged combustion. *Energy* **2020**, *209*, 118480. [CrossRef]
4. Foust, M.; Thomsen, D.; Stickles, R.; Cooper, C.; Dodds, W. Development of the GE Aviation Low Emissions TAPS Combustor for Next Generation Aircraft Engines. In Proceedings of the 50th AIAA Aerospace Sciences Meeting Including the New Horizons Forum & Aerospace Exposition, Nashville, TN, USA, 9–12 January 2012.
5. Wang, Y.; Wu, J.; Lin, Y. Effects of confinement length of the central toroidal recirculation zone partly confined by the small pilot stage chamber on ignition characteristics. *Aerosp. Sci. Technol.* **2020**, *107*, 106277. [CrossRef]
6. Mongia, H. Engineering Aspects of Complex Gas Turbine Combustion Mixers Part II: High T3. In Proceedings of the 49th AIAA Aerospace Sciences Meeting including the New Horizons Forum and Aerospace Exposition (AIAA), Orlando, FL, USA, 4–7 January 2011.
7. Mongia, H. Engineering Aspects of Complex Gas Turbine Combustion Mixers Part III: 30 OPR. In Proceedings of the 9th Annual International Energy Conversion Engineering Conference, San Diego, CA, USA, 31 July–3 August 2011.
8. Mongia, H. Engineering Aspects of Complex Gas Turbine Combustion Mixers Part V: 40 OPR. In Proceedings of the 9th Annual International Energy Conversion Engineering Conference, San Diego, CA, USA, 31 July–3 August 2011.
9. Mongia, H.C. N+3 and N+4 Generation Aeropropulsion Engine Combustors: Part 6: Operating Conditions, Target Goals and Lifted Jets. In Proceedings of the 49th AIAA/ASME/SAE/ASEE Joint Propulsion Conference, San Jose, CA, USA, 14–17 July 2013.
10. Mongia, H.C.; Al-Roub, M.; Danis, A.; Elliott-Lewis, D.; Vise, S. Swirl cup modeling part 1. 2001. In Proceedings of the 37th Joint Propulsion Conference and Exhibit, Salt Lake City, UT, USA, 8–11 July 2001.
11. Lee, C.; Chang, C.T.; Herbon, J.T.; Kramer, S.K. NASA Environmentally Responsible Aviation Project Develops Next-Generation Low-Emissions Combustor Technologies (Phase I). *J. Aeronaut. Aerosp. Eng.* **2013**, *2*, 1000116.
12. Dhanuka, S.K.; Temme, J.E.; Driscoll, J. Unsteady Aspects of Lean Premixed Prevaporized Gas Turbine Combustors: Flame-Flame Interactions. *J. Propuls. Power* **2011**, *27*, 631–641. [CrossRef]
13. Dhanuka, S.K.; Temme, J.E.; Driscoll, J.F.; Mongia, H.C. Vortex-shedding and mixing layer effects on periodic flashback in a lean premixed prevaporized gas turbine combustor. *Proc. Combust. Inst.* **2009**, *32*, 2901–2908. [CrossRef]
14. Dhanuka, S.; Driscoll, J.; Mongia, H. Instantaneous Flow Structures in a Reacting Gas Turbine Combustor. In Proceedings of the 44th AIAA/ASME/SAE/ASEE Joint Propulsion Conference & Exhibit, Hartford, CT, USA, 21–23 July 2008. [CrossRef]
15. Song, H.; Han, X.; Su, T.; Xue, X.; Zhang, C.; Sung, C.J. Parametric study of the slope confinement for passive control in a centrally-staged swirl burner. *Energy* **2021**, *233*, 121188. [CrossRef]
16. Yang, S.; Zhang, C.; Lin, Y.; Xue, X.; Gan, X. Experimental investigation of the ignition process in a separated dual-swirl spray flame. *Combust. Flame* **2020**, *219*, 161–177. [CrossRef]
17. Mi, X.; Zhang, C.; Wang, B.; Lin, Y. Influence of Main Stage Air Splits on the Ignition Performance of TeLESS-II Combustor. In Proceedings of the ASME Turbo Expo 2017: Turbomachinery Technical Conference and Exposition, Charlotte, NC, USA, 26–30 June 2017.
18. Han, X.; Laera, D.; Morgans, A.S.; Sung, C.J.; Hui, X.; Lin, Y.Z. Flame macrostructures and thermoacoustic instabilities in stratified swirling flames. *Proc. Combust. Inst.* **2019**, *37*, 5377–5384. [CrossRef]
19. Dewanji, D.; Rao, A.G.; Pourquie, M.; Van Buijtenen, J.P. Investigation of Flow Characteristics in Lean Direct Injection Combustors. *J. Propuls. Power* **2012**, *28*, 181–196. [CrossRef]
20. Dewanji, D.; Rao, A.G. Spray Combustion Modeling in Lean Direct Injection Combustors, Part I: Single-Element LDI. *Combust. Sci. Technol.* **2015**, *187*, 537–557. [CrossRef]
21. Patel, N.; Menon, S. Simulation of spray–turbulence–flame interactions in a lean direct injection combustor. *Combust. Flame* **2008**, *153*, 228–257. [CrossRef]
22. Patel, N.; Krta, M.; Sankaran, V.; Menon, S. Simulation of spray combustion in a lean-direct injection combustor. *Proc. Combust. Inst.* **2007**, *31*, 2327–2334. [CrossRef]
23. Wang, S.; Yang, V.; Hsiao, G.; Hsieh, S.-Y.; Mongia, H.C. Large-eddy simulations of gas-turbine swirl injector flow dynamics. *J. Fluid Mech.* **2007**, *583*, 99. [CrossRef]
24. Liu, W.; Yang, Q.; Xue, R.; Wang, H. Large Eddy Simulation Study of Flow Dynamics in a Multi-Swirler Model Combustor at Elevated Pressure and High Temperature. *J. Therm. Sci. Eng. Appl.* **2019**, *11*, 1. [CrossRef]
25. Lumley, J.L. *Stochastic Tools in Turbulence*; Academic Press: New York, NY, USA; London, UK, 2007.
26. Sirovich, L. Turbulence and the dynamics of coherent structures. I. Coherent structures. *Q. Appl. Math.* **1987**, *45*, 561–571. [CrossRef]
27. Schmid, P.J.; Sesterhenn, J. Dynamic mode decomposition of numerical and experimental data. *J. Fluid Mech.* **2010**, *656*, 5–28. [CrossRef]
28. Zhang, Z.; Liu, X.; Gong, Y.; Li, Z.; Zheng, H. Investigation on flame characteristics of industrial gas turbine combustor with different mixing uniformities. *Fuel* **2020**, *259*, 116297. [CrossRef]
29. Stopper, U.; Meier, W.; Sadanandan, R.; Stoehr, M.; Aigner, M.; Bulat, G. Experimental Study of Industrial Gas Turbine Flames Including Quantification of Pressure Influence on Flow Field, Fuel/Air Premixing and Flame Shape. *Combust. Flame* **2013**, *160*, 2103–2118. [CrossRef]
30. Durbin, P. Turbulent Flows. By S. B. POPE. *J. Fluid Mech.* **2001**, *427*, 410–411. [CrossRef]

31. Estevadeordal, J.; Gorrell, S.E.; Copenhaver, W.W. PIV Study of Wake-Rotor Interactions in a Transonic Compressor at Various Operating Conditions. *J. Propuls. Power* **2007**, *23*, 235–242. [CrossRef]
32. Jiang, P.; He, X. Performance of a novel mixed-flow trapped vortex combustor for turboshaft engine. *Aerosp. Sci. Technol.* **2020**, *105*, 106034. [CrossRef]
33. Ying, H.; Yang, V. Dynamics and stability of lean-premixed swirl-stabilized combustion. *Prog. Energy Combust. Sci.* **2009**, *35*, 293–364.
34. Huang, D.; Xu, J.; Chen, R.; Meng, H. Large eddy simulations of turbulent combustion of kerosene-air in a dual swirl gas turbine model combustor at high pressures. *Fuel* **2020**, *282*, 118820. [CrossRef]
35. Garci'a-Villalba, M.; FröHlich, J.; Rodi, W. Identification and analysis of coherent structures in the near field of a turbulent unconfined annular swirling jet using large eddy simulation. *Phys. Fluids* **2006**, *18*, 1192–1694.
36. Li, L.; Li, X.; Wang, Z.; Wang, B.; Lin, H.; Hu, W.; Chang, F.; Zhou, B. Experimental investigation of the flow-spray field in a realistic concentric staged high-temperature-rise combustor. *Fuel* **2022**, *318*, 123606. [CrossRef]